





Article

A Geometric Berry Phase Angle Induced in *Im-3m* H₃S at 200 GPa by Ultra-Fast Laser Pulses

Genwei Hong¹, Xinjie Zhou¹, Huan He¹, Tianlv Xu¹, Herbert Früchtl² , Tanja van Mourik² , Yaxin Zhai³, Steven R. Kirk¹  and Samantha Jenkins^{1,*} 

¹ Key Laboratory of Chemical Biology and Traditional Chinese Medicine Research and Key Laboratory of Resource, National and Local Joint Engineering Laboratory for New Petro-Chemical Materials and Fine Utilization of Resources, College of Chemistry and Chemical Engineering, Hunan Normal University, Changsha 410081, China; 202270122575@hunnu.edu.cn (G.H.); 202220122463@hunnu.edu.cn (X.Z.); 202220122456@hunnu.edu.cn (H.H.); steven.kirk@cantab.net (S.R.K.)

² EaStCHEM School of Chemistry, University of St Andrews, North Haugh, St Andrews KY16 9ST, UK

³ Key Laboratory of Low-Dimensional Quantum Structures and Quantum Control of Ministry of Education, Department of Physics, Hunan Normal University, Changsha 410081, China; yzhai@hunnu.edu.cn

* Correspondence: samanthajsuman@gmail.com

Abstract: We investigated *Im-3m* H₃S at 200 GPa, a pressure regime where crystalline H₃S is widely considered to be a superconductor. Simulated circularly polarized 10 femtosecond (fs) laser pulses were applied and we quantified the effects on the electron dynamics both during the application of the ultra-fast laser pulse and 5.0 fs after the pulse was switched off. In addition, the carrier-envelope phase (CEP) angle ϕ , which quantifies the relationship between the time-varying direction of electric (**E**)-field and the amplitude envelope, is employed to control the time evolution of the wavefunction $\psi(\mathbf{r})$. This is undertaken for the first application of Next Generation Quantum Theory of Atoms in Molecules (NG-QTAIM) to the solid state. Ultra-fast phenomena related to superconductivity are discovered in the form of a geometric Berry phase angle associated with the H-H bonding in addition to very high values of the chirality–helicity function that correspond to values normally found in chiral molecules. Future applications are discussed, including chiral spin selective phenomena in addition to high-temperature superconductivity and organic superconductors where phonons do not play a significant role.

Keywords: NG-QTAIM; *Im-3m* H₃S; geometric Berry phase; circularly polarized ultra-fast laser; carrier-envelope phase angle



Academic Editors: Enrico Bodo and Anthony Harriman

Received: 3 January 2025

Revised: 6 February 2025

Accepted: 14 February 2025

Published: 16 February 2025

Citation: Hong, G.; Zhou, X.; He, H.; Xu, T.; Früchtl, H.; van Mourik, T.; Zhai, Y.; Kirk, S.R.; Jenkins, S. A Geometric Berry Phase Angle Induced in *Im-3m* H₃S at 200 GPa by Ultra-Fast Laser Pulses. *Symmetry* **2025**, *17*, 299. <https://doi.org/10.3390/sym17020299>

Copyright: © 2025 by the authors. Licensee MDPI, Basel, Switzerland. This article is an open access article distributed under the terms and conditions of the Creative Commons Attribution (CC BY) license (<https://creativecommons.org/licenses/by/4.0/>).

1. Introduction

The use of compounds containing light elements has provided routes to the discovery of high-temperature superconductors; one such an example is H₃S. In particular, hydrogen-based compounds have been demonstrated to display high-temperature superconductivity subjected to high pressure, offering promise for the fruitful search of metal hydrides' critical temperatures approaching room temperature [1].

It is broadly accepted that H₃S is a superconductor [2], even though there is some skepticism regarding this, on the basis of optical reflectivity experiments [3].

Bardeen–Cooper–Schrieffer (BCS) theory [4], originally created as the universal theory for superconductivity, has long been considered a central pillar of superconductivity investigation [5,6] but universal application has proven to be overly optimistic [7]. In addition, Hirsch argued that BCS theory does not correctly explain the Meissner effect [8], and proposes an alternative to BCS theory, referred to as hole superconductivity [9]. The

need for an alternative theory to BCS [10] was highlighted by the work of Koizumi, who demonstrated that BCS theory does not explain the generation of supercurrents in superconductors. In agreement with Hirsch [11], they argue that standard theory does not account for the reversible superconductor–normal transition found in type I superconductors. The method of Koizumi and Ishikawa also attempts to resolve the problems with BCS theory by using a new supercurrent generation mechanism by utilization of the Berry phase [12]. Mottonen and co-workers determined the Berry phase experimentally in a superconducting charge pump [13].

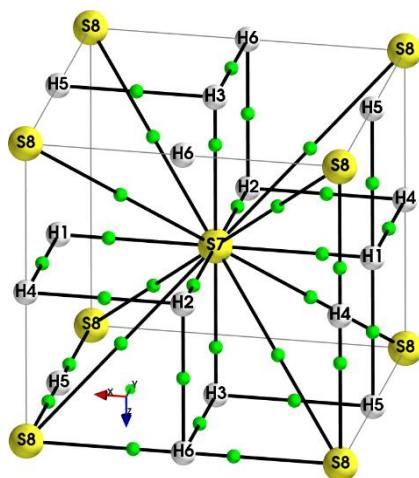
Ultra-fast laser pulses, when applied to a solid, generally create a superposition of excited states whereby the electronic wavefunction evolves on ultra-fast timescales in response to the rapidly changing E-field, both in magnitude and direction, associated with the ultra-fast laser pulses. We note that other works in the field have used ultra-fast laser pulses to induce superconductivity [14].

Recently, the mechanical and chiral properties [15] of ethane were investigated with next generation QTAIM (NG-QTAIM) [16–18] and as ultra-fast laser ‘probes’ [19]. NG-QTAIM [16,17] is the vector-based version of the original QTAIM theory [20]. These investigations of ethane employed electron dynamics generated by simulated pairs of clockwise {(CW), [+1]}, right-handed (**R**) and counter-clockwise {(CCW), [−1]}, left-handed (**S**) circularly polarized non-ionizing ultra-fast laser pulses. In addition, ethane was subjected to linear non-ionizing laser pulses and the effects on the electron dynamics during the application of the ultra-fast laser pulse and in particular after the pulse was switched off were subsequently analyzed using NG-QTAIM [21]. Complementing NG-QTAIM, the circularly polarized pump–probe experimental method is particularly powerful for studying spin dynamics in semiconductors [22]. It provides critical insights into spin polarization and relaxation processes, which are essential for advancing spintronics devices such as spin-LEDs and spin valves [23].

Recently, some of the current authors further investigated the relationship $\rho(\mathbf{r}) \rightarrow \psi(\mathbf{r})$ by subjecting ethane to a pair of simulated left- and right-circularly polarized non-ionizing laser pulses where the inverse mapping $\psi(\mathbf{r}) \rightarrow \rho(\mathbf{r})$ is already understood [24] using scalar quantum chemical theory. This was undertaken by varying the carrier-envelope phase (CEP) angle ϕ of the ultra-fast laser pulses. The CEP angle ϕ is defined to be the phase difference ϕ between the time-dependent phases of the ultra-fast laser pulse ‘envelope’, i.e., it is the time-dependent *scalar* magnitude of the electric (**E**)-field in addition to the time dependent *direction* vector of the electric field associated with the carrier wave, at a reference time. Varying the CEP angle ϕ enables the control of the time evolution of the wavefunction $\psi(\mathbf{r})$. Previously, the CEP angle ϕ has been demonstrated to be central to processes where control of the electron dynamics is vital, where the pulse duration contains only a few optical cycles of the carrier frequency, including photoelectron emission [25], high-order harmonics generation [26], electron localization [27], and electron momentum density [28]. Because the CEP angle ϕ is associated with the direction vector of the ultra-fast laser electric (**E**)-field, the subsequent theoretical analysis necessitates the use of a *vector*-based quantum chemical theory as opposed to conventional *scalar*-based quantum chemical theory.

We do not include phonons or the concept of Cooper pairs in this investigation on ultra-fast timescales. We instead use the total electronic charge density distribution $\rho(\mathbf{r})$, which includes summed spin-up and spin-down $\rho(\mathbf{r})$ contributions. In this investigation of *Im-3m*-H₃S, one goal is to explore the existence of ultra-fast superconductivity effects and any evidence of a non-trivial, i.e., non-zero geometric Berry phase angle. Other goals include the determination of after-pulse effects in addition to learning more about the relationship $\rho(\mathbf{r}) \rightarrow \psi(\mathbf{r})$ towards the eventual aim of the comprehensive ‘reverse engineering’ of ultra-fast laser pulses. This is undertaken by subjecting the *Im-3m*-H₃S to a pair of simulated

circularly polarized non-ionizing ultra-fast laser pulses whilst varying the CEP angle ϕ and including any after-pulse effects, using NG-QTAIM, see Scheme 1.



Scheme 1. The crystal graph of the $Im\text{-}3m\text{-H}_3\text{S}$ unit cell at a pressure of 200 GPa in the yz plane before the pair of circularly polarized ultra-fast laser pulses are applied. Clockwise {CW, [+1], right-handed (R) and counter-clockwise {CCW, [−1], left-handed (S) pulses with peak electric (E)-field strength, $E = 200.0 \times 10^{-4}$ a.u. with carrier-envelope phase angles $\phi = 0^\circ, 30^\circ, 60^\circ, 90^\circ, 120^\circ, 150^\circ, 180^\circ$ are used, see the Computational Details section. Bond critical points (BCPs) are represented by green spheres. Note the inset Cartesian X-Y-Z axes. Before application of the laser pulses, the corresponding interatomic separations are 2.70 a.u., 2.82 a.u., and 4.89 a.u. for the S-H bonds, H-H bonds, and S---S bonds, respectively.

2. Theoretical Background

The backgrounds of QTAIM and next generation QTAIM (NG-QTAIM) along with the calculation procedures are provided in the Supplementary Materials S1. The Kolmogorov-Zurbenko[29] data filter was applied for the smoothing procedure for the calculation of the Hessian of $\rho(\mathbf{r})$ eigenvector-following trajectories $T(s)$

The topology sum rule for the four types of critical points found in infinite solids modeled with periodic boundary conditions is a Morse relation that is sometimes referred to as the Euler–Poincaré relation [30]:

$$n - b + r - c = 0 \quad (1)$$

In Equation (1), n , b , r , and c are the numbers of NCPs, BCPs, RCPs, and CCPs, respectively. We will refer to the collection of all four types of critical points and the associated bond-paths as the *crystal-graph*.

The Hessian of $\rho(\mathbf{r})$ eigenvector-following trajectories $T(s)$ and the U-space distortion set {F, C, A} are created using laser irradiation. For simplicity, from this point onwards, we will refer to the Hessian of $\rho(\mathbf{r})$ eigenvector-following trajectories $T(s)$ as trajectories $T(s)$.

The Hessian of $\rho(\mathbf{r}) \pm \mathbf{e}_1$ and $\pm \mathbf{e}_2$ eigenvectors are orientated in the yz plane of laser polarization, see Scheme 1. The $\pm \mathbf{e}_2$ eigenvector corresponds to the most *facile*, i.e., easier *direction* for BCP electrons to be displaced when the BCP is subjected to a displacement, e.g., a torsion [31]. The bond-flexing F is defined as the difference in the maximum projections (the dot product of the Hessian of $\rho(\mathbf{r}) \mathbf{e}_2$ eigenvector and the BCP displacement \mathbf{dr}) of the $T(s)$ values between the left-handed circularly polarized (S, CCW [+1]) and right-handed circularly polarized (R, CW [−1]) ultra-fast laser pulse:

$$F = [(\mathbf{e}_1 \cdot \mathbf{dr})_{\max}]_{\text{CW}} - [(\mathbf{e}_1 \cdot \mathbf{dr})_{\max}]_{\text{CCW}} \quad (2)$$

The bond-flexing F provides a measure of the ‘flexing-strain’ a bond-path in a crystal graph is under when subject to an external force e.g., an ultra-fast laser pulse, see Equation (2).

The bond-chirality C , is defined as:

$$C = [(\mathbf{e}_2 \cdot \mathbf{dr})_{\max}]_{CW} - [(\mathbf{e}_2 \cdot \mathbf{dr})_{\max}]_{CCW}. \quad (3)$$

The bond-chirality C , see Equation (3), quantifies the *circular BCP* displacement where the corresponding largest magnitude Hessian of $\rho(\mathbf{r})$ eigenvalue (λ_2) is associated with $\pm \mathbf{e}_2$. Recently, the relationship between steric and electronic factors was discovered to be significantly more complex [32] than earlier thought. This was demonstrated for molecular structures for helical electronic transitions of spiroconjugated molecules [33,34].

The bond-axiality A is defined as:

$$A = [(\mathbf{e}_3 \cdot \mathbf{dr})_{\max}]_{CW} - [(\mathbf{e}_3 \cdot \mathbf{dr})_{\max}]_{CCW}. \quad (4)$$

and quantifies the direction of *axial* displacements of *BCPs* in response to the left-handed (\mathbf{S} , CCW [+1]) and right-handed (\mathbf{R} , CW [−1]) circularly polarized ultra-fast laser pulses, i.e., the sliding of the *BCP* along the bond-path [35] within the crystal graph, see Equation (4).

The complete U-space distortion set {bond-flexing F , chirality C , bond axiality A } comprises all three of the Hessian of $\rho(\mathbf{r}) \pm \mathbf{e}_1$, $\pm \mathbf{e}_2$ and $\pm \mathbf{e}_3$ eigenvectors, respectively. The sign (+) or (−) of each of the chirality C , bond-flexing F and bond-axiality A , respectively, determines the presence of \mathbf{S} character for $C > 0$, $F > 0$, or $A > 0$ and \mathbf{R} character for $C < 0$, $F < 0$, or $A < 0$, see Tables 1 and 2.

Table 1. (a). The variation of the *S7-H1 BCP* U-space distortion sets $F = \text{bond-flexing}_{\max}$, $C = \text{bond-chirality}_{\max}$, and $A = \text{bond-axiality}_{\max}$ of the crystal graph of the *Im-3m* H_3S unit cell corresponding to the 5.0 fs peaks for the clockwise (\mathbf{R} , CW [+1]), right-handed (red) and counter-clockwise (\mathbf{S} , CCW [−1]), left-handed (blue) for values of the carrier-envelope phase (CEP) angle $\phi = 0^\circ, 30^\circ, 60^\circ, 90^\circ, 120^\circ, 150^\circ, 180^\circ$ in the planes of polarization yz are provided, see Scheme 1; all entries have been multiplied by 10^3 . Values of the chirality–helicity function $C_{\text{helicity}} = C|A|$ are considered insignificant for values of 1.0×10^{-4} or less. (b). The variation of the *S7-H1 BCP* U-space distortion sets $\{F, C, A\}$ of the crystal graph of the *Im-3m* H_3S unit cell for the variation of the CEP angle ϕ corresponding to 15.0 fs peaks, see (a) for further details.

(a)		
ϕ	$\{F, C, A\}$	C_{helicity}
0°	{−0.00020785, −0.00131086[\mathbf{R}], 0.00479936}	−0.000006
30°	{−0.00164093, 0.00357259[\mathbf{S}], −0.00568488}	0.000020
60°	{0.00001563, −0.00029957[\mathbf{R}], −0.00508324}	−0.000002
90°	{0.00089116, −0.00092710[\mathbf{R}], −0.00387651}	−0.000004
120°	{0.00048556, −0.00059968[\mathbf{R}], −0.00163054}	−0.000001
150°	{0.00048844, 0.00085479[\mathbf{S}], −0.00002236}	0.000000
180°	{−0.00042580, −0.00355555[\mathbf{R}], −0.00312646}	−0.000011

Table 1. Cont.

(b)		
ϕ	{E, C, A}	C_{helicity}
0°	{−0.00141764, −0.00039934[R], −0.00003510}	−0.000000
30°	{0.00406894, 0.00384703[S], −0.00092194}	0.000004
60°	{0.00356699, 0.00273614[S], −0.00096778}	0.000003
90°	{0.00361266, −0.00117082[R], 0.00119853}	−0.000001
120°	{−0.00440098, −0.00844341[R], 0.00028270}	−0.000002
150°	{−0.00079749, −0.00118301[R], −0.00056539}	−0.000001
180°	{−0.00160549, −0.00094371[R], −0.00061383}	−0.000001

Table 2. (a). The variation of the *S7-H3 BCP* U-space distortion sets {E, C, A} of the crystal graph of the *Im-3m* H₃S unit cell for the variation of the CEP angle ϕ corresponding to 5.0 fs peaks, see the caption of Table 1a for further details. (b). The variation of the *S7-H3 BCP* U-space distortion sets {E, C, A} of the crystal graph of the *Im-3m* H₃S unit cell for the variation of the CEP angle ϕ corresponding to 15.0 fs peaks, see the caption of Table 1a for further details.

(a)		
ϕ	{E, C, A}	C_{helicity}
0°	{0.00395620, 0.00068954[S], −0.00541317}	0.00000
30°	{0.00343817, 0.00045152[S], −0.00484821}	0.00000
60°	{−0.00241064, 0.00262590[S], −0.00545623}	0.00001
90°	{−0.00407532, −0.00284361[R], −0.00488540}	−0.00001
120°	{−0.00611005, −0.00015849[R], −0.00263417}	−0.00000
150°	{−0.00683875, −0.00328675[R], −0.00251966}	−0.00001
180°	{−0.00546774, −0.00130459[R], −0.00275087}	−0.00000
(b)		
ϕ	{E, C, A}	C_{helicity}
0°	{−0.00034367, −0.00320850[R], −0.03242285}	−0.00010
30°	{0.00137164, 0.00074987[S], −0.03190550}	0.00002
60°	{−0.00192498, 0.00374808[S], −0.03208291}	0.00012
90°	{−0.00240857, 0.00045161[S], −0.02964950}	0.00001
120°	{−0.00262345, 0.00028611[S], −0.03944482}	0.00001
150°	{−0.00403366, −0.00326675[R], −0.05167981}	−0.00017
180°	{−0.00096860, −0.00348057[R], −0.04446884}	−0.00016

The chirality–helicity function $C_{\text{helicity}} = C |A|$ is the numerical product of the bond-chirality C and the magnitude of the bond-axiality A and was earlier used to determine the nature of any chiral behaviors present in the presence of a pair of left- and right-circularly polarized ultra-fast laser pulses [34]. The helical motion of electrons has long been associated with superconductivity [36]; therefore, we suggest that significant values of the chirality–helicity function C_{helicity} indicate the presence of superconductivity associated with the motion of the electronic charge density $\rho(\mathbf{r}_b)$ at a BCP.

Berry phases, of relevance for superconductivity [12], see the Introduction, possess associated vectors, which, if parallel-transported around a loop and back to the origin, can

acquire an angle, known as a geometric Berry phase angle, with respect to their directions at the origin before transport. Within NG-QTAIM, vectors can also be parallel-transported around a loop back to the origin where the vectors are the points in U-space [16] on a trajectory $T(s)$ where the parallel-transport of the vectors is tracked by the locations of the start (yellow spheres) and end markers (cyan cubes), see Figures 1–5. Within the NG-QTAIM interpretation of Berry phases, a geometric Berry phase angle occurs for a rotation in the $T(s)$ that does not match the change in the CEP angle ϕ . For instance, when the CEP angle ϕ increases from $\phi = 0^\circ$ to $\phi = 180^\circ$, if the $T(s)$ also rotates by 180° , as determined by the positions of the start (yellow spheres) and end (cyan cubes) of the $T(s)$, then there is no associated (non-zero) geometric Berry phase angle, i.e., the geometric Berry phase has vanished, see for example Figure 5. If, however, the rotation of the $T(s)$ is e.g., 90° , whilst the CEP angle ϕ increases from $\phi = 0^\circ$ to $\phi = 180^\circ$, then there is an associated geometric Berry phase angle of 90° , see for example Figure 5.

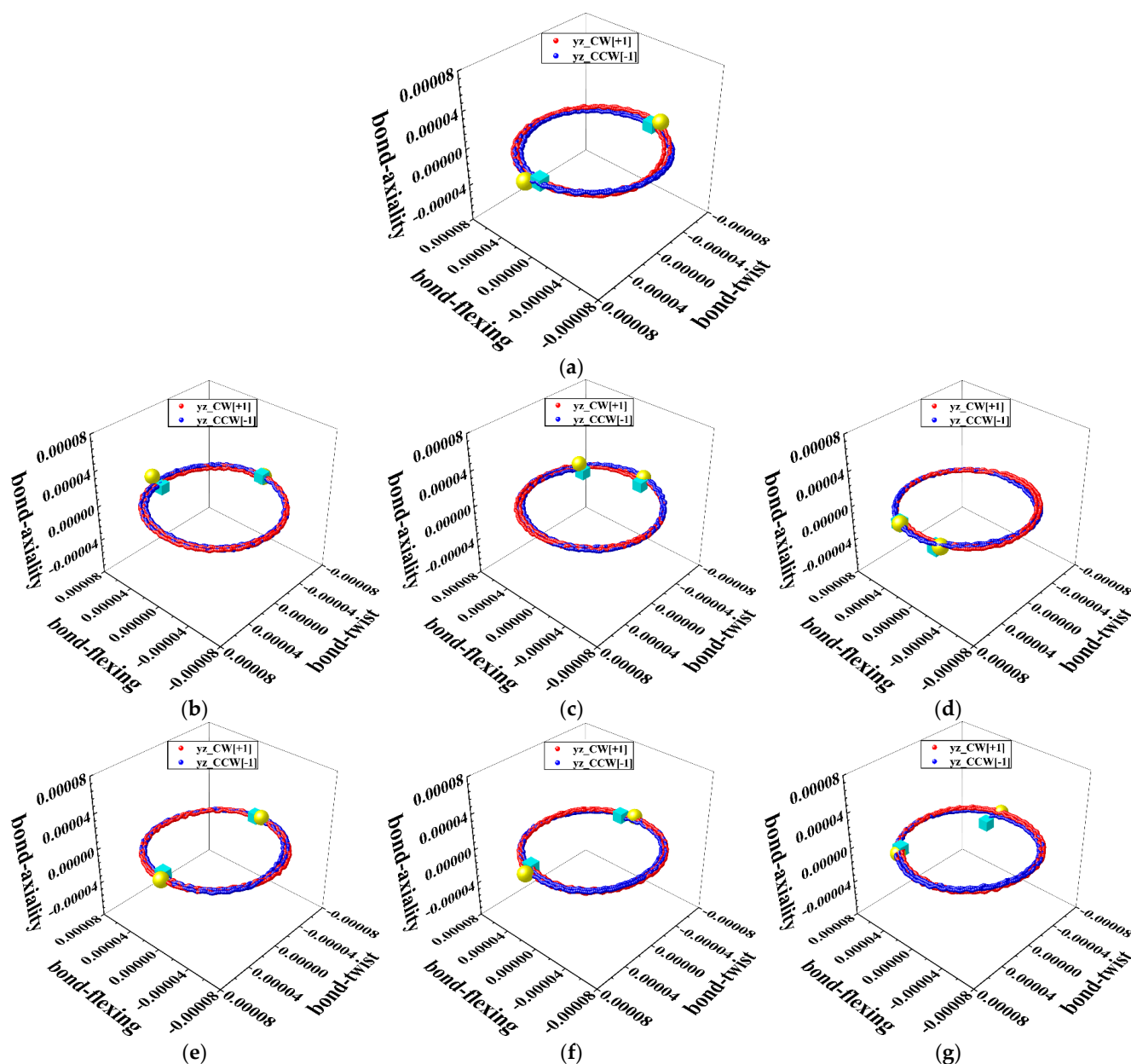


Figure 1. The variation of the $Im-3m$ -H₃S crystal graph S7-H1 BCP trajectories $T(s)$ for 5.0 fs peaks of the clockwise (R, CW [+1]), right-handed (red) and counter-clockwise (S, CCW [−1]), left-handed (blue) circularly polarized ultra-fast laser pulses in the yz plane for the carrier-envelope phase (CEP)

angle $\phi = 0^\circ, 30^\circ, 60^\circ, 90^\circ, 120^\circ, 150^\circ, 180^\circ$ are presented in sub-figures (a–g), respectively. The start and end of each T(s) are denoted by yellow spheres and cyan cubes, respectively.

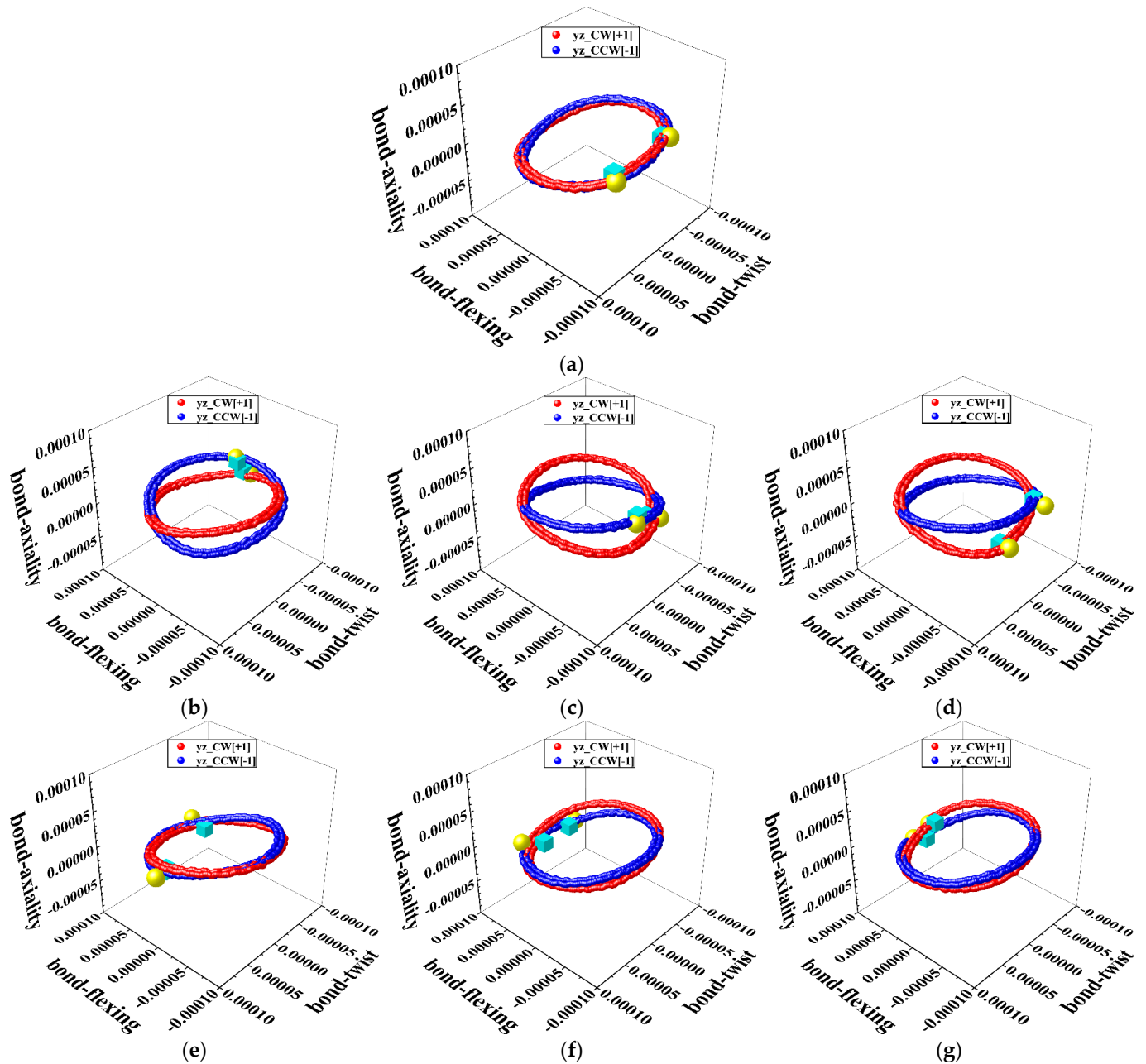


Figure 2. The variation of the $Im-3m$ - H_3S crystal graph S7-H1 BCP trajectories T(s) for 15.0 fs peaks of the CW (R, red) and the CCW (S, blue) circularly polarized ultra-fast laser pulses in the yz plane for the carrier-envelope phase (CEP) angle $\phi = 0^\circ, 30^\circ, 60^\circ, 90^\circ, 120^\circ, 150^\circ, 180^\circ$ are presented in sub-figures (a–g), respectively. See the caption of Figure 1 for further details. The start and end of each T(s) are denoted by yellow spheres and cyan cubes, respectively.

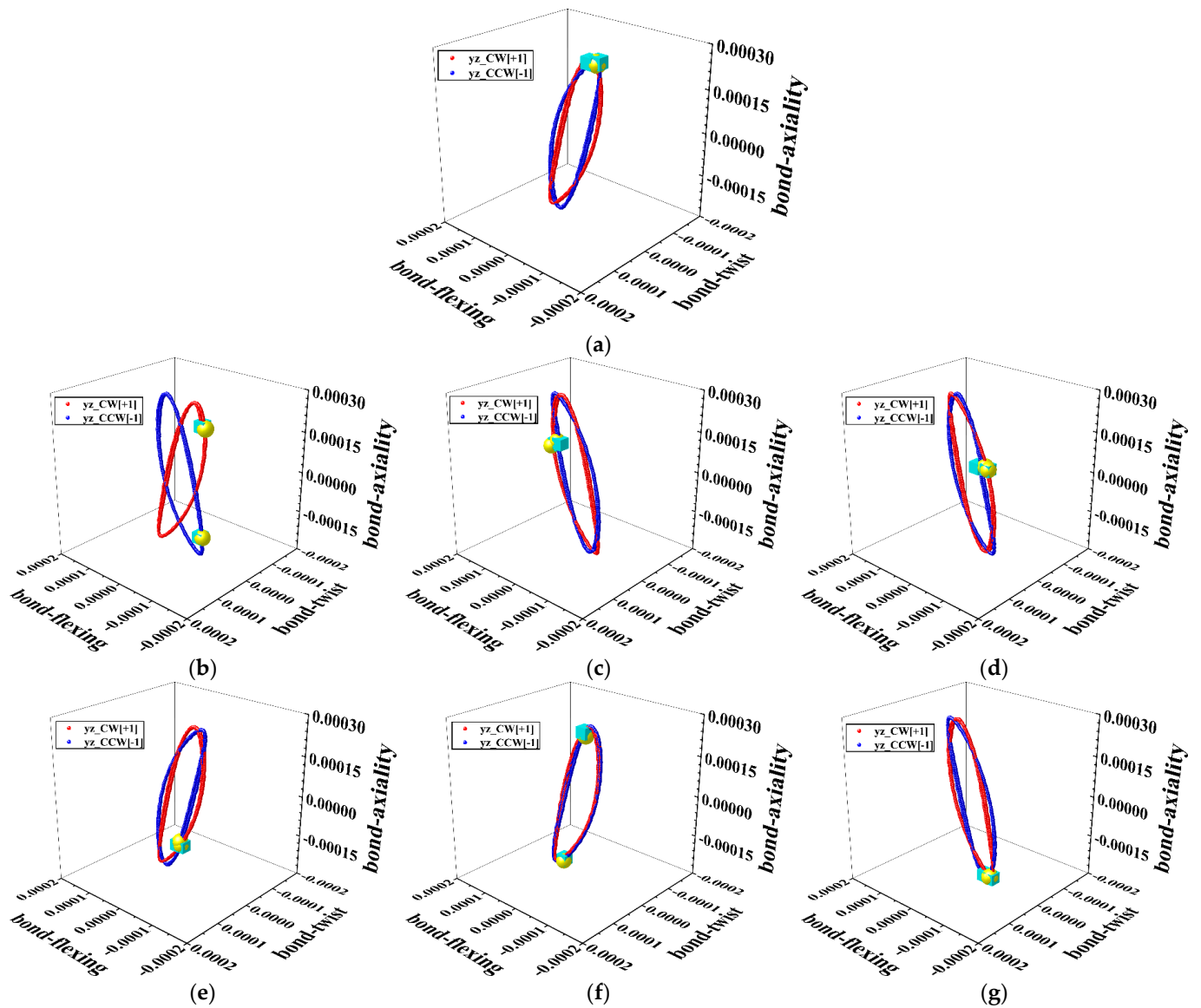


Figure 3. The variation of the $Im-3m-H_3S$ crystal graph S7-H3 BCP trajectories $T(s)$ for 5.0 fs peaks of the CW (R, red) and the CCW (S, blue) circularly polarized ultra-fast laser pulses in the yz plane for the carrier-envelope phase (CEP) angle $\phi = 0^\circ, 30^\circ, 60^\circ, 90^\circ, 120^\circ, 150^\circ, 180^\circ$ are presented in sub-figures (a–g), respectively. The start and end of each $T(s)$ are denoted by yellow spheres and cyan cubes, respectively.

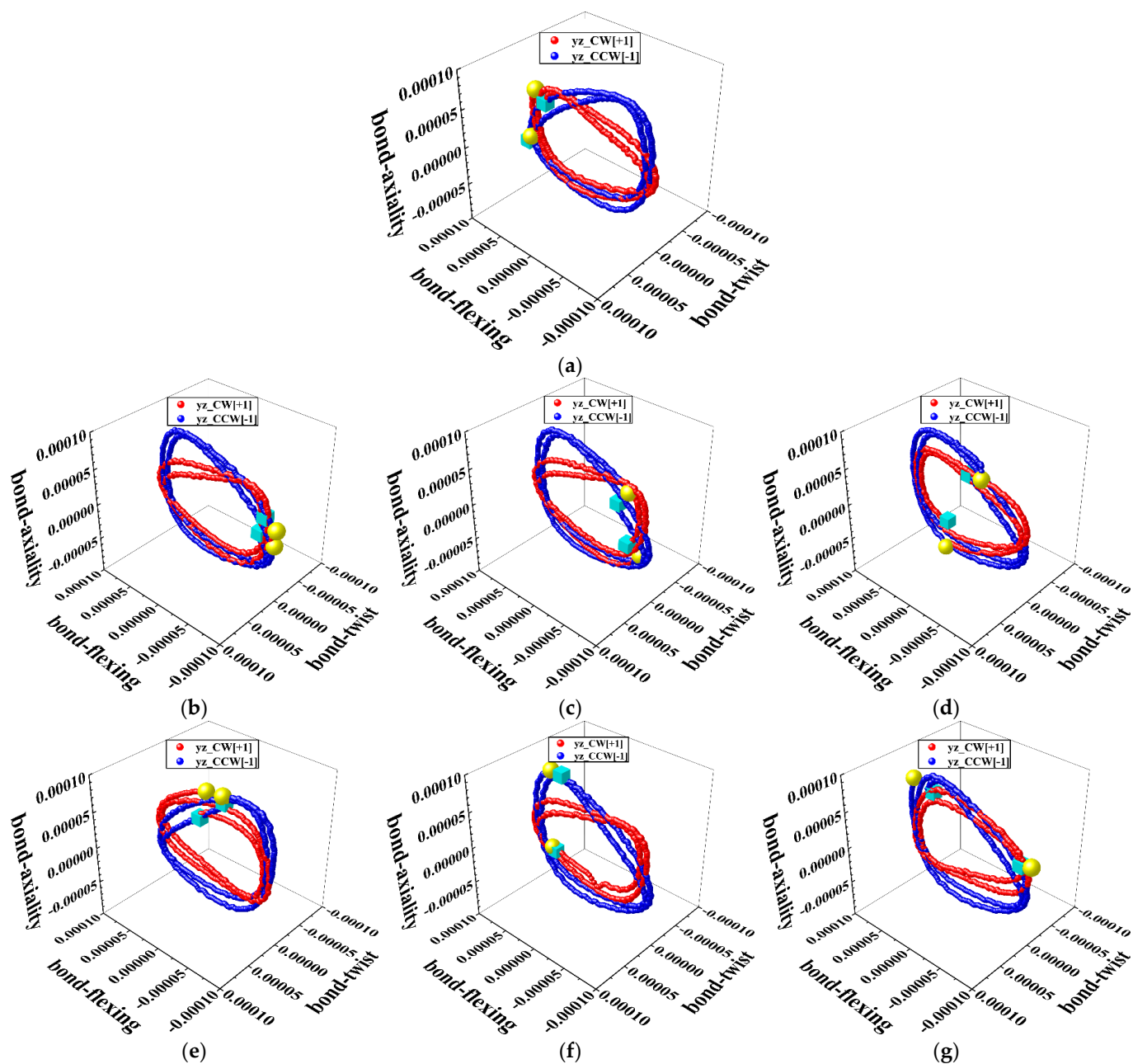


Figure 4. The variation of the $Im\text{-}3m\text{-H}_3\text{S}$ crystal graph S7-H3 BCP trajectories $T(s)$ for 15.0 fs peaks of the CW (R, red) and the CCW (S, blue) circularly polarized ultra-fast laser pulses in the yz plane for the CEP angle $\phi = 0^\circ, 30^\circ, 60^\circ, 90^\circ, 120^\circ, 150^\circ, 180^\circ$ are presented in sub-figures (a–g), respectively. For further details, see Figure 3.

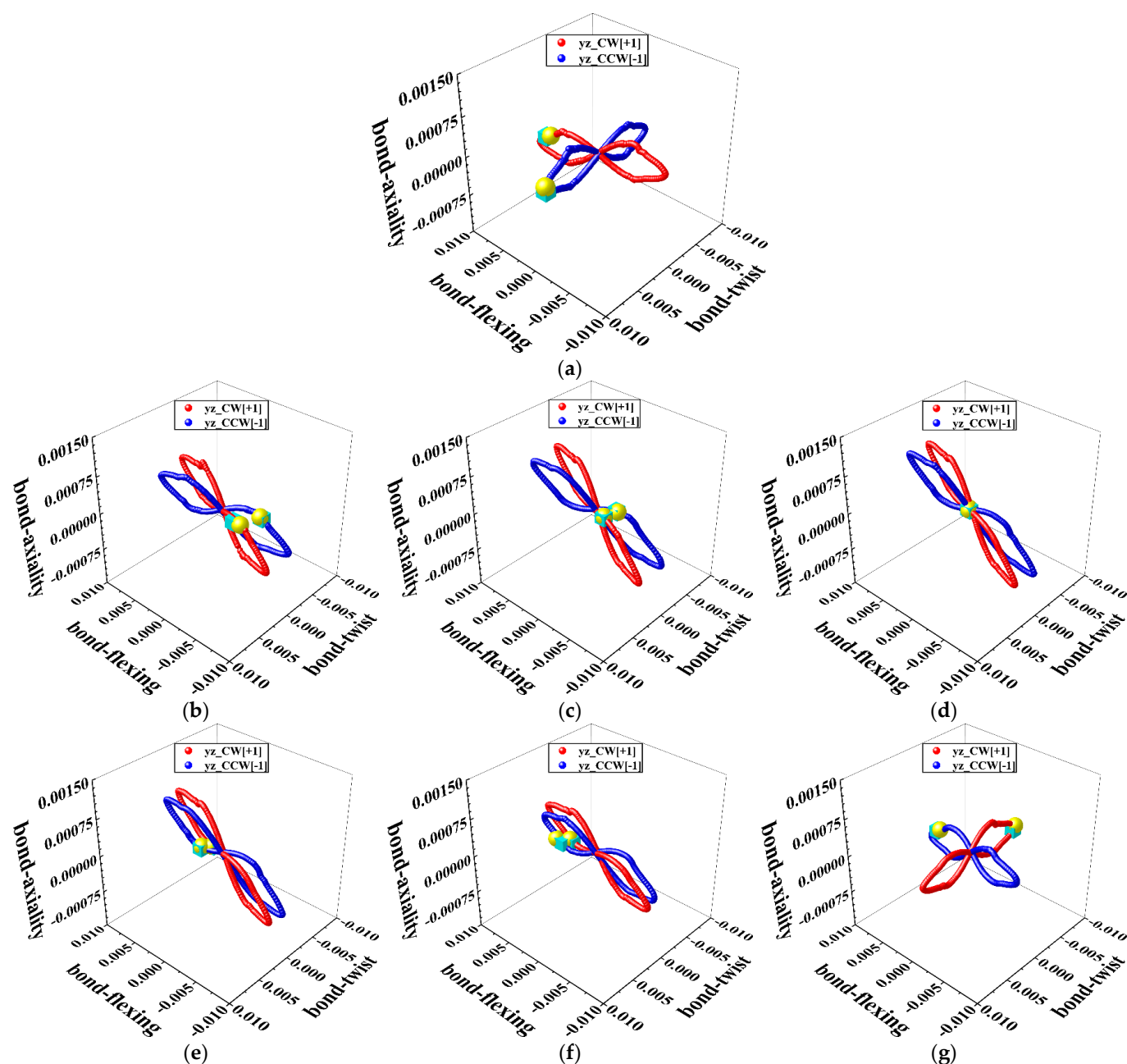


Figure 5. The variation of the $Im\text{-}3m\text{-H}_3\text{S}$ crystal graph H3–H5 BCP trajectories $T(s)$ for 5.0 fs peaks of the CW (R, red) and the CCW (S, blue) circularly polarized ultra-fast laser pulses in the yz plane for the carrier-envelope phase (CEP) angle $\phi = 0^\circ, 30^\circ, 60^\circ, 90^\circ, 120^\circ, 150^\circ, 180^\circ$ are presented in sub-figures (a–g), respectively. The start and end of each $T(s)$ are denoted by yellow spheres and cyan cubes, respectively.

3. Computational Details

The $Im\text{-}3m$ H_3S unit cell was first geometry-optimized at 200 GPa isostatic pressure and zero applied external electric (\mathbf{E})-field. This was carried out using the CASTEP version 23.1 [37] implementation of the RSCAN DFT meta-GGA functional [38] using generated Koelling–Harmon pseudopotentials, ‘fine’ basis set accuracy, a plane-wave basis set cutoff of 462.5936 eV with a total energy/atom convergence tolerance of 10^{-5} eV, Fermi smearing width 0.2 eV, a $25 \times 25 \times 25$ Monkhorst–Pack k-point grid with a (0.01, 0.01, 0.01) offset and a total energy convergence tolerance of 2×10^{-5} eV/atom with the LBFGS minimization algorithm. The resulting equilibrium lattice parameter $a = 2.986656 \text{ \AA}$ was used in subse-

quent calculation steps. The nuclear coordinates are fixed during the ultra-fast electron dynamics calculation; hence, no nuclear lattice temperature is defined.

The electron dynamics propagation was carried out with the Octopus code [39] using a spinor wavefunction representation, spin-orbit coupling, and the nuclear positions fixed. The initial ground-state wavefunction was calculated using a random starting magnetization density, HGH pseudopotentials, and LDA with an RMMDIIS eigensolver tolerance of 1.0×10^{-7} and a relative density convergence criterion of 1.0×10^{-6} . A mesh spacing of 0.05 \AA was used. An additional 10 states were converged, with Fermi–Dirac smearing of 0.1 eV , on a $4 \times 4 \times 4$ grid with relaxation of symmetry constraints allowed in the two orthogonal directions (y and z) comprising the intended plane of rotation of the ultra-fast laser electric field vector. Propagation of the electron dynamics was then carried out using the Approximated Enforced Time-Reversal Symmetry (AETRS) propagator with the Lanczos method for the exponential of the Hamiltonian and an exponential order of 16, using a time step of 0.03 a.u. This value of the timestep was found to be the largest possible value that maintained numerical stability throughout the propagation.

From the start of the electron dynamics calculation, corresponding to $t = 0$ onwards, an external time-dependent electric field vector $\mathbf{E}(t)$ was imposed to model a single 10.0 fs duration ‘sine-squared’-shaped circularly polarized ultra-fast laser pulse with peak amplitude $\mathbf{E} = 200 \times 10^{-4} \text{ a.u.}$ This pulse was simulated using time-dependent electric field components $[\mathbf{E}_y(t), \mathbf{E}_z(t)]$ in the yz polarization plane, see the crystal coordinate axes as defined in Scheme 1. The overall field vector $[\mathbf{E}_y(t), \mathbf{E}_z(t)]$ was computed as the product of the following three terms:

1. The ‘carrier’ wave, starting at time $t = 0 \text{ fs}$ with an initial phase set to the desired CEP angle ϕ , defined to be the vector $[\sin(\omega t + \phi), \sin(\omega t + \phi + \pi/2)]$ in the (y, z) polarization plane with selected laser pulse excitation frequency ω .
2. An ‘envelope’ of amplitude corresponding to a single laser pulse as a half-cycle ‘sine-squared’ function $\mathbf{E}_{\text{peak}} \sin^2(\omega_{\text{env}} t)$, also starting at time $t = 0$ with phase = 0° and peak field amplitude $\mathbf{E}_{\text{peak}} = 200 \times 10^{-4} \text{ a.u.}$ and with ω_{env} selected to result in a half-cycle, i.e., single laser pulse, duration of 10.0 fs .
3. A ‘polarization’ factor of $+1$ or -1 , applied uniquely to the \mathbf{E}_z -field component. This yielded an electric field \mathbf{E} vector, which turned either clockwise {CW, $+1$ } and right-handed (**R**) or counter-clockwise {CCW, -1 } and left-handed (**S**) in the (y, z) plane of polarization where the NG-QTAIM **R** and **S** chirality assignments are denoted by a bold font. Given the short (10.0 fs) duration of the pulse, a ‘field broadening’ approach to constructing the time-evolving superposition of excited states was employed: in the special case of a ‘ \sin^2 ’ amplitude envelope function pulse of duration ΔT the energetic ‘broadening’ was induced by the field is $\Delta E = \hbar/\Delta T$. Such short duration pulses are energetically broad, hence also unselective. Therefore, a carrier frequency (excitation energy) of frequency $\omega = 0.350 \text{ a.u.}$ for the ultra-fast laser pulse was thus chosen to cover a relatively broad range of possible lower-lying excited states.

Dynamics runs were then performed for values of the CEP angle $\phi = 0^\circ, 30^\circ, 60^\circ, 90^\circ, 120^\circ, 150^\circ,$ and 180° . ‘Timeslices’ corresponding to two full cycles of the ultra-fast laser pulse excitation carrier frequency were then defined within each dynamics run. The first timeslice was ‘centered’ on $t = 5.0 \text{ fs}$, i.e., from just before to just after the time corresponding to the peak magnitude of the electric (\mathbf{E}) field associated with the ultra-fast laser pulse. Additional timeslices of the same duration, i.e., two carrier cycles, were defined centered on $t = 15.0 \text{ fs}$, i.e., after the magnitude of the electric field associated with the 10.0 fs laser pulse had dropped to zero. Within each timeslice, ‘snapshot’ grids of charge density were saved every two propagation timesteps, with the total charge density being reconstructed from the sum of the ‘spin-up’ and ‘spin-down’ densities output by the Octopus code. The

BCPs, bond-paths, and eigenvectors of the Hessian of the electronic charge density $\rho(\mathbf{r})$ were then extracted from the gridded total charge density distribution using the CRITIC2 code [40] with the ‘density-smoothing’ [41] option and with core densities re-added, while ensuring that the Euler–Poincaré relationship, see Equation (1), was satisfied throughout. NG-QTAIM properties were then obtained using the in-house QuantVec [42] suite that is compatible with CRITIC2 outputs. For each ‘timeslice’, the trajectories $T(s)$ were then calculated, taking particular care to correctly track critical points shifting across the periodic boundaries of the unit cell.

4. Results and Discussion

In this first investigation using NG-QTAIM in the solid state, we use circularly polarized ultra-fast laser pulses of duration 10 fs to induce the electron dynamics of the *Im-3m* H₃S crystal graph. The effect of the right-handed (**R**, CW [+1]) and left-handed (**S**, CCW [−1]) circularly polarized ultra-fast laser pulse in the *yz* plane on the electron dynamics is quantified at the mid-way point (5.0 fs) of the 10.0 fs pulse and after the pulse is switched off at 15.0 fs, see Scheme 1. Before the application of the ultra-fast laser pulses, in the *yz* plane, the corresponding interatomic (geometric) separations (GPLs) are 2.70 a.u., 2.82 a.u., and 4.89 a.u. for the S–H BCPs, H–H BCPs, and S–S BCPs, respectively, see the Supplementary Materials S2. Note that we use the bond notation “--” and “---” to denote the H–H BCPs and S–S closed shell BCPs where the Laplacian $\nabla^2\rho(\mathbf{r}_b) > 0$, indicating lower concentrations of $\rho(\mathbf{r}_b)$ than for BCPs with Laplacian $\nabla^2\rho(\mathbf{r}_b) < 0$, conventionally described as stronger bonds such as the shared-shell S–H BCPs of this investigation; the subscript “**b**” indicates a BCP. We also adopt the convention of the reference time being defined as the start time of the ultra-fast laser pulse, refer to the Section 3.

We investigate both the S7–H1 BCP and S7–H3 BCP because their associated bond-paths are perpendicular to the *yz* plane and in the *yz* plane, respectively, of the ultra-fast laser pulses, see Scheme 1. Note that **S** and **R** denote electronic stereoisomers. A bold font is used to indicate their vector-based NG-QTAIM origin and that they do not refer to conventional geometric structural stereoisomers.

Comparisons of the S7–H1 BCP and S7–H3 BCP ellipticity ε for the mid-pulse (5.0 fs) and at 15 fs, i.e., 5.0 fs after the 10.0 fs pulse is removed of the right-handed (**R**) and left-handed (**S**) circularly polarized ultra-fast laser pulses are provided in the Supplementary Materials S3. The remaining plots for the variation of the ellipticity ε with time for the H3–H5 BCP and S7–S8 BCP are provided in the Supplementary Materials S3. It is observed that the **S** and **R** S7–H3 BCP ellipticity ε at 5.0 fs possess smooth sinusoidal-type variations with time and are almost indistinguishable. We note that this is very similar to the corresponding ellipticity ε plots for the ethane C–C BCP [15]. The **S** and **R** S7–H3 BCP ellipticity ε values possess a shift of a quarter of a cycle relative to each other at 15.0 fs. The reverse occurs during and after the pulse with similar shifts for the S7–H1 BCP. We also notice that for the S7–H1 BCP, ellipticity ε values decrease after the ultra-fast laser pulses are removed, whereas the converse is true for the S7–H3 BCP ellipticity ε values.

The use of the ellipticity ε was found to be problematic for the closed-shell H–H BCPs and closed-shell S–S BCPs, resulting in significant numbers of scattered data values due to numerical noise. This scatter in the ellipticity ε values corresponds to low values of $\rho(\mathbf{r}_b) = 0.056$ a.u., for both the closed-shell H–H BCPs and closed-shell S–S BCPs, compared with the higher value of $\rho(\mathbf{r}_b) = 0.1587$ a.u. for the shared-shell S–H BCP. The BCP ellipticity ε , a scalar, however, only provides *partial* symmetry breaking and therefore cannot provide directional information associated with the response of the electron dynamics at a BCP to the ultra-fast lasers due to the lack of full symmetry-breaking [43].

These limitations of the use of the *BCP* ellipticity ε can be overcome by the inclusion of the $\pm\mathbf{e}_1$, $\pm\mathbf{e}_2$ and $\pm\mathbf{e}_3$ eigenvectors undertaken with calculation of the Hessian of $\rho(\mathbf{r})$ eigenvector-trajectories $T(s)$ that are generated by the applied circularly polarized ultra-fast laser pulses, see Figures 1–5. The corresponding maximum trajectory projections $T_{\max}(s)$ values are provided in the Supplementary Materials S4. All of the $T(s)$ in this investigation associated with the *S-H BCPs* and *H-H BCPs* are smooth and continuous during the ultra-fast laser pulses and after they are removed. The corresponding values for the much longer (4.89 a.u.) *S---S BCPs*, however, are not; therefore, we only include the results within the duration of the pulse. The $T(s)$ results associated with the *S7---S8 BCP* are provided in the Supplementary Materials S5.

The morphology of the $T(s)$ of the **S** and **R** stereoisomers during the pulse depends on the orientation of the *S-H BCP* bond-path relative to the yz plane of the applied laser pulses. The $T(s)$ associated with the *S7-H1 BCP* bond-path were perpendicular to the yz plane and possessed a high degree of circular character, see Figures 1 and 2. Conversely, the *S7-H3 BCP* bond-path is orientated parallel to the yz plane and possesses a high degree of elliptical character, see Figures 3 and 4. There is no concerted shift in the $T(s)$ of the **S** and **R** stereoisomers as the CEP angle is varied from $\phi = 0^\circ$ and 180° for the *S7-H1 BCP*, see Figure 1a–g. After the ultra-fast laser pulse is removed, the $T(s)$ of the **S** and **R** stereoisomers uncoil somewhat, see Figure 2.

Conversely, the tightly coiled $T(s)$ of the *S7-H3 BCP* of the **S** and **R** stereoisomers undergo a rigid shift of 180° as the CEP angle is varied from $\phi = 0^\circ$ to 180° , as can be observed by comparing the positions of the start (yellow spheres) and end markers (cyan cubes), from the top to the bottom, see the Section 2 and compare Figure 3a with Figure 3g. The geometric Berry Phase has vanished since there is a geometric Berry phase angle of 0° . For the *S7-H3 BCP*, a clear shift of the $T(s)$ of the **S** and **R** stereoisomers is observed for a value of the CEP angle $\phi = 30^\circ$, see Figure 3b. After the pulse is removed, the $T(s)$ of the *S7-H3 BCP* **S** and **R** stereoisomers uncoil for all values of the CEP angle ϕ and the rigid 180° shift of the $T(s)$ is no longer present, see Figure 4.

The U-space distortion sets F , C , and A are very low for all values of the CEP angle ϕ for the $T(s)$ associated with the *S7-H1 BCP* and *S7-H3 BCP*; however, the values of A increase by an order of magnitude for the *S7-H3 BCP* after the pulses are removed, see Tables 1 and 2, respectively. The values of the chirality–helicity function C_{helicity} are therefore quantified as insignificant for all values of the CEP angle ϕ at the mid-pulse (5.0 fs) and after the ultra-fast laser pulse is removed.

The **S** and **R** trajectories $T(s)$ for the *H3--H5 BCP*, at the mid-point (5.0 fs) of the pulse, all possess an unusual bowtie morphology, see Figure 5. After the pulse is removed (15.0 fs), the bowtie morphology is deformed to form an “x” morphology, see Supplementary Materials S4. There is a smooth progression of the position of the start (yellow spheres) and end (cyan cubes) markers of the $T(s)$, at the mid-point (5.0 fs) of the pulse, as the CEP angle ϕ is increased from $\phi = 30^\circ$ to 150° , see Figure 2b–f, respectively. At $\phi = 90^\circ$, which corresponds to the mid-point of the variation of the CEP ϕ , both sets of markers are located at the geometric center of both the **S** and **R** trajectories $T(s)$, see Figure 5d. The *H3--H5 BCP* **S** and **R** $T(s)$ rotate by 90° , whilst the CEP angle ϕ increases from $\phi = 0^\circ$ to $\phi = 180^\circ$, which means that there is an associated geometric Berry phase angle of 90° .

After the pulse is removed, there is no longer an ordered progression of the positions of the start and end markers and therefore no geometric Berry phase angle.

The chirality C assignment reverses from **S** to **R**, for the mid-pulse, for a value of $\phi = 180^\circ$, see Table 3a. After the pulse, the chirality C assignment reverses from **S** to **R** twice. These reversals occur for values of CEP angle $\phi = 30^\circ$ and $\phi = 150^\circ$, coinciding with large reductions in the value of the chirality C , see Table 3b.

Table 3. (a). The variation of the H3--H5 BCP U-space distortion sets {F, C, A} of the crystal graph of the *Im-3m* H₃S unit cell for the variation of the CEP angle ϕ corresponding to 5.0 fs peaks, see the caption of Table 1a for further details. (b). The variation of the H3--H5 BCP U-space distortion sets {F, C, A} of the crystal graph of the *Im-3m* H₃S unit cell for the variation of the CEP angle ϕ corresponding to 15.0 fs peaks, see (a) for further details.

(a)		
ϕ	{F, C, A}	C_{helicity}
0°	{15.36881044, −14.1175355[R], 0.04852940}	−0.68512
30°	{0.39218615, −2.01422662[R], 0.18215077}	−0.36689
60°	{0.79557267, −2.49460523[R], −0.02143174}	−0.05346
90°	{0.29057790, −1.85751870[R], −0.08630643}	−0.16032
120°	{−0.03259674, −0.43128741[R], 0.03124769}	−0.01348
150°	{0.14292926, −0.34667352[R], 0.17702022}	−0.06137
180°	{−14.91095652, 13.3962577[S], −0.15900106}	2.13002
(b)		
ϕ	{F,C, A}	C_{helicity}
0°	{0.02449043, −0.01165811[R], −0.00350769}	−0.00004
30°	{−0.01882514, 0.00855684[S], −0.00096604}	0.00001
60°	{−0.02982649, −0.05461642[R], 0.00031557}	−0.00002
90°	{−0.03078349, −0.00723467[R], 0.00461964}	−0.00003
120°	{0.00291624, −0.01300193[R], 0.00413865}	−0.00005
150°	{−0.03170038, 0.00312240[S], 0.00225964}	0.00001
180°	{0.46458456, −0.46008490[R], 0.00312497}	0.00144

The bond-flexing F and bond-axiality A values are extremely high at the mid-pulse for values of the CEP angle $\phi = 0^\circ$ and $\phi = 180^\circ$, two orders of magnitude greater than for the remaining values of the CEP angle ϕ . For the mid-pulse, the chirality C and the bond-axiality A result in high values of the chirality–helicity function C_{helicity} for all values of the CEP angle ϕ , in particular for $\phi = 180^\circ$.

After the ultra-fast laser pulses are removed for all values of the CEP angle ϕ , there are insignificant values of the chirality–helicity function C_{helicity} , with the exception of the CEP angle $\phi = 180^\circ$.

5. Conclusions

In this investigation, we applied pairs of left- and right-circularly polarized non-ionizing ultra-fast laser pulses of duration 10.0 fs with peak E-field ($E = 200.0 \times 10^{-4}$ a.u.) to the *Im-3m* H₃S crystal graph whilst varying the carrier-envelope phase (CEP) angle ϕ . We quantified the response of the electron dynamics at the mid-pulse (5.0 fs) and at 15.0 fs, corresponding to 5.0 fs after the ultra-fast laser pulses were removed.

The form of the time variations of the ellipticity ϵ values of the **S** and **R** stereoisomers were found to depend on the orientation of the S-H BCP bond-path relative to the plane (*yz* plane) of the applied laser pulses. The ellipticity ϵ , however, proved troublesome for the analysis of the electron dynamics associated with the closed shell H3--H5 BCP and S7---S8 BCP due to numerical noise.

The morphology of the T(s) of the **S** and **R** stereoisomers also depended on the orientation of the S-H BCP bond-path relative to the plane of the applied laser pulses.

The $T(s)$ associated with the S7-H1 BCP bond-path were perpendicular to the yz plane and possessed a high degree of circular character. Conversely, the S7-H1 BCP bond-paths were parallel to the yz plane and possessed a high degree of elliptical character, not to be confused with the ellipticity ε . The presence of a clear shift of the $T(s)$ of the **S** and **R** stereoisomers for the S7-H3 BCP for a value of the CEP angle $\phi = 30^\circ$ suggests that ultra-fast laser pulses can be used to separate the **S** and **R** stereoisomers, indicating the future potential for use in stereoselectivity applications. The $T(s)$ of the **S** and **R** stereoisomers were found recognizable although somewhat ‘uncoiled’ (S-H BCPs) or distorted (H3--H5 BCP) after the ultra-fast laser pulses were removed for all values of the CEP angle ϕ .

The trajectories $T(s)$ with the U-space distortion set {F,C,A} revealed and quantified the complete absence of significant chiral character for the S-H BCPs, determined from the value of the chirality–helicity function $C_{\text{helicity}} = 0$ for all values of the peak E-field, in agreement with a conventionally achiral molecule and our previous investigation of ethane [15]. Conversely, the value of the chirality–helicity function C_{helicity} for the H3--H5 BCP during the pulse was very high where reversals in the **S** to **R** chirality C assignments were found to be present. The use of the symmetry-breaking U-space within NG-QTAIM enabled the location of a non-zero geometric Berry phase angle of 90° for the $T(s)$ associated with the **S** and **R** stereoisomers of the H3--H5 BCP. We hypothesize that the very high values of the chirality–helicity function C_{helicity} , and the geometric Berry phase angle of 90° for the $T(s)$ associated with the **S** and **R** stereoisomers of the H3--H5 BCP, are both indicators of superconductivity on the ultra-fast time-scale. The insights gained in this investigation using the variation of the CEP angle ϕ with ultra-fast lasers pulse have therefore demonstrated the potential for the use of NG-QTAIM for use in reverse engineering laser parameters via the relationship $\rho(\mathbf{r}) \rightarrow \Psi(\mathbf{r})$.

Currently, work is underway using ultra-fast laser irradiation to construct ultra-fast laser probes, where nuclei are free to move but not given enough time to respond to the ultra-fast laser pulses. The use of a probe laser pulse will enable a better understanding of the true nature of the superconductivity within the NG-QTAIM interpretation and how the response changes with the application laser pulses with higher peak E-fields. This is being undertaken by using lower peak E-fields, e.g., $E = 5.0 \times 10^{-4}$ a.u. up to 20.0×10^{-4} a.u. on the electron dynamics that will be analyzed using the $T(s)$ along with the NG-QTAIM interpretation of the chemical bond [43], see the Section 1.

NG-QTAIM could be used to consider the mechanism of high-temperature superconductors, where phonons play almost no role and so will be excluded. Instead, the mechanism of high-temperature superconductivity is assumed to be governed by spin-density waves, which we therefore plan to investigate by constructing $T(s)$ each from spin-up and spin-down contributions to $\rho(\mathbf{r})$. Since phonons are not relevant, this approach can also be considered for organic superconductors [44].

Current densities could in future be used to construct $T(s)$ to enable direct detection of the ring currents that are associated with superconductors. Plans for NG-QTAIM also include the use of a U-space current density trajectory $T(s)$ including explicit spin-up and spin-down contributions to $\rho(\mathbf{r})$ for chiral spin selectivity to inform experiment for room-temperature spin light-emitting diodes [23,45–49].

NG-QTAIM is as important as circularly polarized pump–probe experiments, as both provide complementary insights into spin dynamics and mutually support each other. By constructing $T(s)$ trajectories with spin-up and spin-down contributions to $\rho(\mathbf{r})$, NG-QTAIM will be used to provide a detailed understanding of spin polarization, coherence, and relaxation processes, similar to what is revealed by pump–probe techniques. In organic semiconductors, it will be used to explain phenomena such as chiral-induced spin selectivity (CISS) and spin-density waves, while in perovskites, it elucidates the effects of spin-orbit

coupling and structural asymmetry on spin behavior. Together, these approaches deliver a comprehensive framework for analyzing transient spin polarization and spin lifetime, which is critical for advancing spintronic devices like spin-LEDs and spin valves. This synergy between NG-QTAIM theory and experiment has the potential to significantly enhance the development of next-generation spintronic technologies.

Supplementary Materials: The following supporting information can be downloaded at: <https://www.mdpi.com/article/10.3390/sym17020299/s1>, **S1.** NG-QTAIM theoretical background and procedure to generate the Hessian of $\rho(r)$ eigenvector-following trajectories $T(s)$; **S2.** Hessian of $\rho(r)$ partitioning scheme scalar QTAIM measures for the 200 GPa Im-3m-H3S crystal graph; **S3.** Variation of the 200 GPa Im-3m-H3S crystal graph ellipticity ε with time and the carrier-envelope phase (CEP) angle ϕ ; **S4.** Tables and trajectories $T(s)$ of the 200 GPa Im-3m-H3S crystal graph; **S5.** Tables and trajectories $T(s)$ of the 200 GPa Im-3m-H3S crystal graph S7--S8 BCP.

Author Contributions: Conceptualization, S.J.; Methodology, S.J.; Software, S.R.K.; Validation, X.Z.; Formal analysis, S.J.; Investigation, S.J.; Resources, S.J.; Data curation, G.H., X.Z., H.H. and T.X.; Writing—original draft, S.J.; Writing—review & editing, H.F., T.v.M., Y.Z. and S.J.; Supervision, T.X. and S.J.; Project administration, S.J. All authors have read and agreed to the published version of the manuscript.

Funding: The Hunan Natural Science Foundation of China project, approval number: 2022JJ30029 and 2023ZJ1010, is gratefully acknowledged. The One Hundred Talents Foundation of Hunan Province is also gratefully acknowledged for the support of S.J. and S.R.K. The use of SHARCNET computing facilities is acknowledged through the auspices of our sponsor, Paul W. Ayers.

Data Availability Statement: Data can be shared on reasonable request.

Acknowledgments: Graeme Ackland is acknowledged for providing the Im-3m H₃S crystal structure and for advice on cell geometry optimizations under isostatic pressure using CASTEP code.

Conflicts of Interest: The authors declare no conflicts of interest.

References

1. Yu, J.; Yong, X.; Liu, H.; Lu, S. Prediction of Enhanced Superconductivity in Cyclo-H₁₂Bi/Pb Involving a Resonant Hydrogen Structure. *Phys. Rev. B* **2024**, *110*, 224507. [[CrossRef](#)]
2. Drozdov, A.P.; Erements, M.I.; Troyan, I.A.; Ksenofontov, V.; Shylin, S.I. Conventional Superconductivity at 203 Kelvin at High Pressures in the Sulfur Hydride System. *Nature* **2015**, *525*, 73–76. [[CrossRef](#)] [[PubMed](#)]
3. Hirsch, J.E.; Marsiglio, F. Evidence Against Superconductivity in Flux Trapping Experiments on Hydrides Under High Pressure. *J. Supercond. Nov. Magn.* **2022**, *35*, 3141–3145. [[CrossRef](#)]
4. Bardeen, J.; Cooper, L.N.; Schrieffer, J.R. Theory of Superconductivity. *Phys. Rev.* **1957**, *108*, 1175–1204. [[CrossRef](#)]
5. van de Bund, S.; Ackland, G.J. Competition between Superconductivity and Molecularization in the Quantum Nuclear Behavior of Lanthanum Hydride. *Phys. Rev. B* **2023**, *108*, 184102. [[CrossRef](#)]
6. Seeyangnok, J.; Hassan, M.M.U.; Pinsook, U.; Ackland, G.J. Superconductivity and Electron Self-Energy in Tungsten-Sulfur-Hydride Monolayer. *2D Mater.* **2024**, *11*, 025020. [[CrossRef](#)]
7. Hirsch, J.E. Superconducting Materials: Judge and Jury of BCS-Electron-Phonon Theory. *Appl. Phys. Lett.* **2022**, *121*, 080501. [[CrossRef](#)]
8. Hirsch, J.E. Superconducting Materials: The Whole Story. *J. Supercond. Nov. Magn.* **2020**, *33*, 61–68. [[CrossRef](#)]
9. Hirsch, J.E. Hole Superconductivity. *Phys. Lett. A* **1989**, *134*, 451–455. [[CrossRef](#)]
10. Koizumi, H. Supercurrent and Electromotive Force Generations by the Berry Connection from Many-Body Wave Functions. *J. Phys. Math. Theor.* **2023**, *56*, 185301. [[CrossRef](#)]
11. Hirsch, J.E. Momentum of Superconducting Electrons and the Explanation of the Meissner Effect. *Phys. Rev. B* **2017**, *95*, 014503. [[CrossRef](#)]
12. Berry, M.V. Quantal Phase Factors Accompanying Adiabatic Changes. *Proc. R. Soc. Lond. Math. Phys. Sci.* **1997**, *392*, 45–57. [[CrossRef](#)]
13. Mottonen, M.; Vartiainen, J.J.; Pekola, J.P. Experimental Determination of the Berry Phase in a Superconducting Charge Pump. *Phys. Rev. Lett.* **2008**, *100*, 177201. [[CrossRef](#)] [[PubMed](#)]

14. Cavalleri, A. Photo-Induced Superconductivity. *Contemp. Phys.* **2018**, *59*, 31–46. [[CrossRef](#)]
15. Mi, X.P.; Lu, H.; Xu, T.; Früchtl, H.; van Mourik, T.; Paterson, M.J.; Kirk, S.R.; Jenkins, S. Response of the Mechanical and Chiral Character of Ethane to Ultra-Fast Laser Pulses. *J. Comput. Chem.* **2023**, *45*, 150–158. [[CrossRef](#)] [[PubMed](#)]
16. Kirk, S.R.; Jenkins, S. Tools for Overcoming Reliance on Energy-Based Measures in Chemistry: A Tutorial Review. *Chem. Soc. Rev.* **2023**, *52*, 5861–5874. [[CrossRef](#)]
17. Jenkins, S.; Kirk, S.R. *Next Generation Quantum Theory of Atoms in Molecules: From Stereochemistry to Photochemistry and Molecular Devices*, Lecture Notes in Chemistry, 1st ed.; Springer Nature: Singapore, 2023; ISBN 978-981-99-0328-3.
18. Koch, D.; Pavanello, M.; Shao, X.; Ihara, M.; Ayers, P.W.; Matta, C.F.; Jenkins, S.; Manzhos, S. The Analysis of Electron Densities: From Basics to Emergent Applications. *Chem. Rev.* **2024**, *124*, 12661–12737. [[CrossRef](#)] [[PubMed](#)]
19. He, H.; Peng Mi, X.; Zhou, X.; Hong, G.; Xu, T.; Früchtl, H.; van Mourik, T.; Paterson, M.J.; Kirk, S.R.; Jenkins, S. Ultra-Fast Laser Pulses as a Probe of Electron Dynamics: A next Generation QTAIM Perspective. *Chem. Phys. Lett.* **2023**, *835*, 141018. [[CrossRef](#)]
20. Bader, R.F.W. *Atoms in Molecules: A Quantum Theory, 1st Paperback ed.*; Clarendon Press: Oxford, UK; New York, NY, USA, 1994; ISBN 978-0-19-855865-1.
21. Lu, H.; Azizi, A.; Mi, X.; Yu, W.; Peng, Y.; Xu, T.; Früchtl, H.; van Mourik, T.; Kirk, S.R.; Jenkins, S. Scoring Molecular Wires Subject to an Ultra-Fast Laser Pulse for Molecular Electronic Devices. *J. Comput. Chem.* **2023**, *44*, 1776–1785. [[CrossRef](#)] [[PubMed](#)]
22. Chen, X.; Lu, H.; Wang, K.; Zhai, Y.; Lunin, V.; Sercel, P.C.; Beard, M.C. Tuning Spin-Polarized Lifetime in Two-Dimensional Metal-Halide Perovskite through Exciton Binding Energy. *J. Am. Chem. Soc.* **2021**, *143*, 19438–19445. [[CrossRef](#)] [[PubMed](#)]
23. Kim, Y.-H.; Zhai, Y.; Lu, H.; Pan, X.; Xiao, C.; Gaulding, E.A.; Harvey, S.P.; Berry, J.J.; Vardeny, Z.V.; Luther, J.M.; et al. Chiral-Induced Spin Selectivity Enables a Room-Temperature Spin Light-Emitting Diode. *Science* **2021**, *371*, 1129–1133. [[CrossRef](#)] [[PubMed](#)]
24. Frenking, G. The Chemical Bond—An Entrance Door of Chemistry to the Neighboring Sciences and to Philosophy. *Isr. J. Chem.* **2022**, *62*, e202100070. [[CrossRef](#)]
25. Dey, D.; Ray, D.; Tiwari, A.K. Controlling Electron Dynamics with Carrier-Envelope Phases of a Laser Pulse. *J. Phys. Chem. A* **2019**, *123*, 4702–4707. [[CrossRef](#)] [[PubMed](#)]
26. Ishii, N.; Kaneshima, K.; Kitano, K.; Kanai, T.; Watanabe, S.; Itatani, J. Carrier-Envelope Phase-Dependent High Harmonic Generation in the Water Window Using Few-Cycle Infrared Pulses. *Nat. Commun.* **2014**, *5*, 3331. [[CrossRef](#)]
27. Lan, P.; Takahashi, E.J.; Liu, K.; Fu, Y.; Midorikawa, K. Carrier Envelope Phase Dependence of Electron Localization in the Multicycle Regime. *New J. Phys.* **2013**, *15*, 063023. [[CrossRef](#)]
28. Lefebvre, C.; Gagnon, D.; Fillion-Gourdeau, F.; MacLean, S. Carrier-Envelope Phase Effects in Graphene. *JOSA B* **2018**, *35*, 958–966. [[CrossRef](#)]
29. Yang, W.; Zurbenko, I. Kolmogorov–Zurbenko Filters. *Wiley Interdiscip. Rev. Comput. Stat.* **2010**, *2*, 340–351. [[CrossRef](#)]
30. Johnson, C.K.; Burnett, M.; Dunbar, W. Crystallographic Topology and Its Applications. In Proceedings of the Crystallographic Computing 7, Bellingham WA, USA, 17–22 August 1996; International Union of Crystallography: Bellingham WA, USA, 1996; pp. 1–25.
31. Szarek, P.; Sueda, Y.; Tachibana, A. Electronic Stress Tensor Description of Chemical Bonds Using Nonclassical Bond Order Concept. *J. Chem. Phys.* **2008**, *129*, 094102. [[CrossRef](#)]
32. Harper, K.C.; Sigman, M.S. Three-Dimensional Correlation of Steric and Electronic Free Energy Relationships Guides Asymmetric Propargylation. *Science* **2011**, *333*, 1875–1878. [[CrossRef](#)] [[PubMed](#)]
33. Garner, M.H.; Corminboeuf, C. Helical Electronic Transitions of Spiroconjugated Molecules. *Chem. Commun.* **2021**, *57*, 6408–6411. [[CrossRef](#)] [[PubMed](#)]
34. Xing, H.; Azizi, A.; Momen, R.; Xu, T.; Kirk, S.R.; Jenkins, S. Chirality–Helicity of Cumulenes: A Non-Scalar Charge Density Derived Perspective. *Int. J. Quantum Chem.* **2022**, *122*, e26884. [[CrossRef](#)]
35. Tian, T.; Xu, T.; Kirk, S.R.; Rongde, I.T.; Tan, Y.B.; Manzhos, S.; Shigeta, Y.; Jenkins, S. Intramolecular Mode Coupling of the Isotopomers of Water: A Non-Scalar Charge Density-Derived Perspective. *Phys. Chem. Chem. Phys.* **2020**, *22*, 2509–2520. [[CrossRef](#)] [[PubMed](#)]
36. Bulaevski, L.N.; Rusinov, A.I.; Kulić, M. Helical Order of Spins in Superconductors. *Solid State Commun.* **1979**, *30*, 59–63. [[CrossRef](#)]
37. Clark, S.J.; Segall, M.D.; Pickard, C.J.; Hasnip, P.J.; Probert, M.I.J.; Refson, K.; Payne, M.C. First Principles Methods Using CASTEP. *Z. Für Krist.—Cryst. Mater.* **2005**, *220*, 567–570. [[CrossRef](#)]
38. Bartók, A.P.; Yates, J.R. Regularized SCAN Functional. *J. Chem. Phys.* **2019**, *150*, 161101. [[CrossRef](#)] [[PubMed](#)]
39. Tancogne-Dejean, N.; Oliveira, M.J.T.; Andrade, X.; Appel, H.; Borca, C.H.; Le Breton, G.; Buchholz, F.; Castro, A.; Corni, S.; Correa, A.A.; et al. Octopus, a Computational Framework for Exploring Light-Driven Phenomena and Quantum Dynamics in Extended and Finite Systems. *J. Chem. Phys.* **2020**, *152*, 124119. [[CrossRef](#)] [[PubMed](#)]
40. Otero-de-la-Roza, A.; Johnson, E.R.; Luaña, V. Critic2: A Program for Real-Space Analysis of Quantum Chemical Interactions in Solids. *Comput. Phys. Commun.* **2014**, *185*, 1007–1018. [[CrossRef](#)]

41. Otero-de-la-Roza, A. Finding Critical Points and Reconstruction of Electron Densities on Grids. *J. Chem. Phys.* **2022**, *156*, 224116. [[CrossRef](#)]
42. Kirk, S.R.; Jenkins, S. QuantVec. 2021. Available online: <https://doi.org/10.5281/zenodo.5553686> (accessed on 21 December 2024).
43. Kirk, S.R.; Jenkins, S. Beyond Energetic and Scalar Measures: Next Generation Quantum Theory of Atoms in Molecules. *WIREs Comput. Mol. Sci.* **2022**, *12*, e1611. [[CrossRef](#)]
44. Clark, K.; Hassanien, A. Superconductivity in Just Four Pairs of (BETS)₂GaCl₄ Molecules. *Nat. Nanotechnol.* **2010**, *5*, 261–265. [[CrossRef](#)] [[PubMed](#)]
45. Naaman, R.; Waldeck, D.H. Spintronics and Chirality: Spin Selectivity in Electron Transport Through Chiral Molecules. *Annu. Rev. Phys. Chem.* **2015**, *66*, 263–281. [[CrossRef](#)] [[PubMed](#)]
46. Naaman, R.; Paltiel, Y. Chiral Molecules and the Electron Spin. *Nat. Rev. Chem.* **2019**, *3*, 250–260. [[CrossRef](#)]
47. Wang, Z.; Gao, M.; Ren, S.; Hao, X.; Qin, W. Magnetic and Electric Control of Circularly Polarized Emission through Tuning Chirality-Generated Orbital Angular Momentum in Organic Helical Polymeric Nanofibers. *Adv. Mater.* **2019**, *31*, 1904857. [[CrossRef](#)] [[PubMed](#)]
48. Kan, Y.; Andersen, S.K.H.; Ding, F.; Kumar, S.; Zhao, C.; Bozhevolnyi, S.I. Metasurface-Enabled Generation of Circularly Polarized Single Photons. *Adv. Mater.* **2020**, *32*, 1907832. [[CrossRef](#)]
49. Long, G.; Jiang, C. Spin Control in Reduced-Dimensional Chiral Perovskites. *Nat. Photonics* **2018**, *12*, 528–533. [[CrossRef](#)]

Disclaimer/Publisher’s Note: The statements, opinions and data contained in all publications are solely those of the individual author(s) and contributor(s) and not of MDPI and/or the editor(s). MDPI and/or the editor(s) disclaim responsibility for any injury to people or property resulting from any ideas, methods, instructions or products referred to in the content.